Frido: Feature Pyramid Diffusion for Complex Scene Image Synthesis

Wan-Cyuan Fan[1*], Yen-Chun Chen[2†],
Dongdong Chen[2], Yu Cheng[2], Lu Yuan[2], Yu-Chiang Frank Wang[1]

[1]National Taiwan University [2]Microsoft Corporation
{wancyuan, ycwang}@ntu.edu.tw
{yen-chun.chen, dochen, yu.cheng, luyuan}@microsoft.com

Abstract

Diffusion models (DMs) have shown great potential for high-quality image synthesis. However, when it comes to producing images with complex scenes, how to properly describe both image global structures and object details remains a challenging task. In this paper, we present *Frido*, a **F**eatur**e** Py**r**am**i**d **D**iffusi**o**n model performing a multi-scale coarse-to-fine denoising process for image synthesis. Our model decomposes an input image into scale-dependent vector quantized features, followed by a coarse-to-fine gating for producing image output. During the above multi-scale representation learning stage, additional input conditions like text, scene graph, or image layout can be further exploited. Thus, *Frido* can be also applied for conditional or cross-modality image synthesis. We conduct extensive experiments over various unconditioned and conditional image generation tasks, ranging from text-to-image synthesis, layout-to-image, scene-graph-to-image, to label-to-image. More specifically, we achieved state-of-the-art FID scores on five benchmarks, namely layout-to-image on COCO and OpenImages, scene-graph-to-image on COCO and Visual Genome, and label-to-image on COCO.[1]

1 Introduction

Generating photo-realistic images is a critical task in computer vision research. In this task, a generative model is designed to learn the underlying data distribution of a given set of images and to be capable of synthesizing new samples from the learned distribution. To this end, series of methods were proposed, including VAEs (Kingma and Welling 2014; Van Den Oord, Vinyals et al. 2017), GANs (Goodfellow et al. 2014; Radford, Metz, and Chintala 2015), flow-based methods (Dinh, Krueger, and Bengio 2014; Kingma and Dhariwal 2018), and the trending diffusion models (DMs) (Sohl-Dickstein et al. 2015; Ho, Jain, and Abbeel 2020). The quality of the generated images has been improved rapidly with the contribution of these lines of works. Moreover, the task itself also evolves from object-centric image synthesis without conditions to complex scene image generation, and sometimes based on multi-modal conditions (e.g., texts, layouts, labels, and scene-graphs).

---
*work done during research internship at Microsoft
†project lead
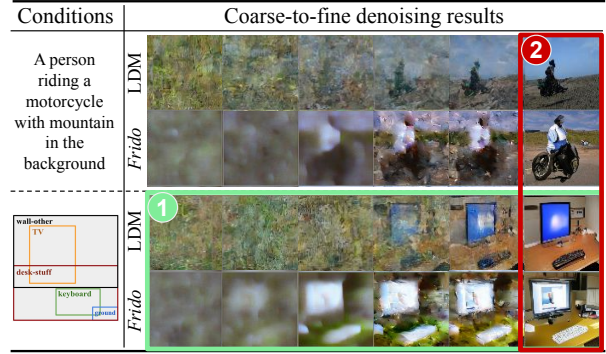[1]Code is available at https://github.com/davidhalladay/Frido.

Figure 1: Illustration of *Frido*. Given a cross-modal condition, *Frido* generates images in ① a coarse-to-fine manner from structure to object details, producing outputs with ② high semantic correctness and quality. Note that existing models such as the LDMs are not designed to distinguish between high/low-level visual information.

Recently, diffusion models (Ho, Jain, and Abbeel 2020; Nichol and Dhariwal 2021; Ho et al. 2022; Rombach et al. 2022; Ramesh et al. 2022) have demonstrated a remarkable capability of high-quality image synthesis and outperform other classes of generative approaches on multiple tasks, including but not limited to unconditional image generation, text-to-image generation, and image super-resolution. Despite the encouraging progress, diffusion models may fall short when targeted images are more complex and conditioning inputs are highly abstractive. The composition of objects and parts, along with high-level semantic relations are prevailing in those tasks, which are less seen in earlier object-centric benchmarks and may be essential to higher quality generation.

In particular, we point out two major challenges in existing DM works. *First*, most of existing DMs deal with feature maps or image pixels at a single scale/resolution, which might not be able to capture image semantics or compositions in real-world complex scenes. Take the first row of Figure 1 as examples, it can be seen that while LDM (Rombach et al. 2022) generates images containing a "person" given the text condition, semantic structures of "riding a motorcycle" and "mountain in the background" are not sufficiently produced. *Second*, expensive computational resources are typically required for DMs during training and testing due

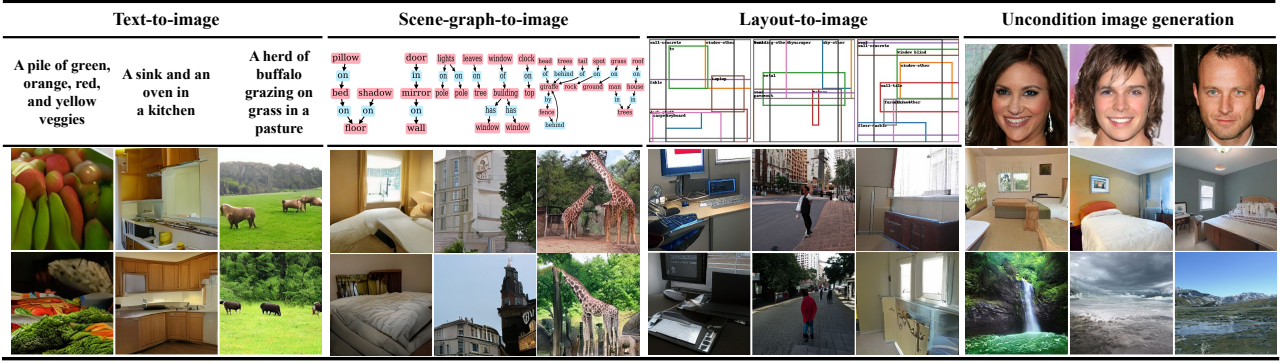| Text-to-image	Scene-graph-to-image	Layout-to-image	Uncondition image generation

Figure 2: Generated examples of *Frido* on various tasks. From left to right, we show the examples of text-to-image (T2I) on COCO 2014, scene-graph-to-image (SG2I) on Visual Genome, layout-to-image (Layout2I) on COCO-stuff, unconditional image generation on Landscape, CelebA, LSUN-bed. All images are 256x256 resolution. Note that, for conditional generation, we adopt classifier-free guidance with s=1.5 while testing. Please refer to supplementary for full-scale version.

to the iterative denoising processes, especially for producing high-resolution outputs. This not only limits the accessibility but also results in massive carbon emissions. Therefore, a computationally efficient diffusion model that leverages coarse/high-level synthesized outputs for introducing multi-scale visual information would be desirable.

To address these limitations, we propose *Frido*, a **F**eature **P**yram**id** **D**iffusi**o**n model for complex scene image generation.[2] *Frido* is a novel multi-scale coarse-to-fine diffusion and denoising framework, which allows synthesizing images with enhanced global structural fidelity and realistic object details. Specifically, we introduce a novel *feature pyramid U-Net* (PyU-Net) with a *coarse-to-fine gating* design, enabling our model to denoise visual features from multiple spatial scales in a top-down fashion. These multi-scale features are produced by our MS-VQGAN, a newly designed multi-scale variant of VQGAN (Esser, Rombach, and Ommer 2021) that encodes images into multi-scale visual features (discrete latent codes). As can be seen in Figure 1, as the feature gradually being denoised, the images are reconstructed in a coarse-to-fine manner (decoded by our MS-VQGAN decoder), from global structures to fine-grained details. On the other hand, a recent competitive diffusion model (Rombach et al. 2022) reconstructs images uniformly across spatial scales.

Frido is a generic diffusion framework that can synthesize images from diverse, multi-modal inputs, including texts, box-layouts, scene-graphs, and labels. Moreover, our model introduces minimal extra parameters while allowing us to speed up the notoriously slow inference of conventional DMs. Extensive experiments are done to demonstrate the effectiveness of the new designs. Our contributions are summarized as follows. (*i*) We propose *Frido*, a novel diffusion model to generate photo-realistic images from multi-modal inputs, with a *coarse-to-fine* prior that is under-explored in the DM paradigm. (*ii*) Empirically, we achieve *5 new state-of-the-art* results, including layout-to-image on COCO and OpenImages, scene-graph-to-image on COCO and Visual Genome, and label-to-image on COCO, all are complex scenes with highly abstractive conditions. (*iii*) In practice,

---

[2]*Frido* is pronounced as "free-dow".

Frido inferences fast, shown by a head-to-head comparison with an already fast diffusion model, the LDM.

2 Preliminary

Multiple lines of works to generate photo-realistic images have been proposed, including VAEs, GANs, and Invertible-Flows, and achieved impressive results for object-centric images. However, VAEs suffer from blurry outputs. GANs are notoriously hard to train and lack diversity. Flow-based model suffers shape distortions due to imperfect inverse transform. Our work belongs to the paradigm of diffusion models (DMs), which have been shown to best synthesize high quality images among all deep generative methods. For completeness, we summarize the fundamentals of DMs and a recent improvement, Latent Diffusion Models (LDMs) (Rombach et al. 2022).

Diffusion Models for Image Generation A diffusion model (DM) contains two stages: forward (diffusion) and backward (denoising) processes. In the forward process, the given data $\mathbf{x}_0 \sim q(\mathbf{x}_0)$ is gradually destroyed into an approximately standard normal distribution $\mathbf{x}_T \sim p(\mathbf{x}_T)$ over T steps.[3] The diffusion process, formulated by Ho, Jain, and Abbeel (2020), are shown as follows:[4]

$$q(\mathbf{x}_{1:T}|\mathbf{x}_0) = \prod_{t=1}^{T} q(\mathbf{x}_t|\mathbf{x}_{t-1}), \text{ and}$$
$$q(\mathbf{x}_t|\mathbf{x}_{t-1}) = \mathcal{N}(\sqrt{1-\beta_t}\mathbf{x}_{t-1}, \beta_t\mathbf{I}). \tag{1}$$

By reversing the forward process, Ho, Jain, and Abbeel (2020) obtained the backward process:

$$p_\theta(\mathbf{x}_{0:T}) = p(\mathbf{x}_T) \prod_{t=1}^{T} p_\theta(\mathbf{x}_{t-1}|\mathbf{x}_t), \text{ and}$$
$$p_\theta(\mathbf{x}_{t-1}|\mathbf{x}_t) = \mathcal{N}(\mathbf{x}_{t-1}; \mu_\theta(\mathbf{x}_t, t), \sigma_\theta(\mathbf{x_t}, t)). \tag{2}$$

---

[3]q and p denote the given data manifold and the standard Gaussian distribution, respectively; and $\mathbf{x}$ denotes a data point from q.

[4]β denotes the noise schedule. Can be fixed or learned.

This is implemented by a neural network predicting each of the denoising steps;[5] and it can be viewed as a Markov chain with a learned Gaussian transition distribution (Dhariwal and Nichol 2021; Pandey et al. 2022).

In practice, we randomly sample a timestep t in $[0, T]$, and then compute $\mathbf{x}_t$.[6] The denoising network ϵ_θ is trained by the following loss:

$$\mathcal{L}_{DM} = \mathbb{E}_{\mathbf{x}_0, \epsilon, t} \left[\|\epsilon - \epsilon_\theta(\mathbf{x}_t)\|^2 \right]. \qquad (3)$$

At a higher level, this loss trains the network to predict the step noise ϵ applied on $\mathbf{x}_{t-1}$ given $\mathbf{x}_t$. To synthesize an image, one can run this denoising network for T steps to gradually denoise a random noise image.

Latent Diffusion Models   Most DMs (Nichol et al. 2022; Dhariwal and Nichol 2021) operate on the original image pixels, yielding high dimensional data manifold with input $\mathbf{x}_0 \in \mathcal{R}^{3 \times H \times W}$. Such high-dimensional inputs cost huge computation for the diffusion and denoising processes at both training and inference. Very recently, Latent Diffusion Models (LDMs) (Rombach et al. 2022) are proposed to adopt DMs to learn the low-dimensional latent codes, encoded by a VQGAN (Esser, Rombach, and Ommer 2021) or KL-autoencoder (Rombach et al. 2022). Given an image $\mathbf{x}_0$ and the pre-trained autoencoder, containing encoder $\mathcal{E}$ and decoder $\mathcal{D}$, the corresponding latent codes $\mathbf{z}_0 = \mathcal{E}(\mathbf{x}_0)$ can be produced.[7] By replacing the image data point $\mathbf{x}$ in Eq. (1) and Eq. (2) with the encoded latent $\mathbf{z}$, the diffusion and denoising processes of a LDM can be derived:

$$q(\mathbf{z}_{1:T} | \mathbf{z}_0) = \prod_{t=1}^{T} q(\mathbf{z}_t | \mathbf{z}_{t-1}), \text{ and}$$

$$p_\theta(\mathbf{z}_{0:T}) = p(\mathbf{z}_T) \prod_{t=1}^{T} p_\theta(\mathbf{z}_{t-1} | \mathbf{z}_t). \qquad (4)$$

At inference, the final output image can be reconstructed from the denoised latent $\tilde{\mathbf{x}}_0 = \mathcal{D}(\tilde{\mathbf{z}}_0)$.[8] Since T is typically set to $500 - 1000$ in practice, and the autoencoding is a one-time operation per image, the overall computation is greatly reduced due to the much lower resolution of $\mathbf{z}_0$.

3   Methodology

Although existing DMs generate high-resolution images for a single object with outstanding quality, most of them only deal with feature maps or image pixels at a single resolution. Since they treat high and low-level visual concepts equally, it is not easy for such DM models to describe the corresponding image semantics or composition. This might limit their uses for synthesizing complex scene images.

To enhance DMs with global structural modeling, we propose to model the latent features in a coarse-to-fine fashion via feature pyramids. We first introduce the Multi-Scale Vector Quantization model (MS-VQGAN), which encodes the image into latent codes at several spatial levels. Next, we propose the feature pyramid diffusion model (*Frido*), extending the diffusion and denoising into a multi-scale, coarse-to-fine fashion. To achieve these, we design a new feature Pyramid U-Net (PyU-Net), equipped with a special gating mechanism to allow coarse-to-fine learning. In this section, we introduce each component in detail.

3.1   Learning Multi-Scale Perceptual Latents

Before we model an image in a coarse-to-fine fashion, we first encode it into latent codes with several spatial resolutions. Extending from VQGAN (Esser, Rombach, and Ommer 2021), we train a multi-scale auto-encoder, named MS-VQGAN, with a feature pyramid encoder $\mathcal{E}$ and decoder $\mathcal{D}$. As shown in Figure 3a, given an image $\mathbf{x}_0$, the encoder $\mathcal{E}$ first produces a latent feature map set of N scales $\mathcal{Z} = \mathcal{E}(\mathbf{x}_0) = \{\mathbf{z}^{1:N}\}$.[9] In this design, we are encouraging $\mathbf{z}^1$ to preserve lower-level visual details and $\mathbf{z}^N$ to represent higher-level shape and structures. Secondly, a decoder $\mathcal{D}$ jointly observes feature maps $\mathcal{Z}$ from all scales and reconstruct the image $\mathcal{D}(\mathcal{Z}) = \tilde{\mathbf{x}}_0$. The objective for this autoencoder module is the weighted sum of l_2 loss between $\mathbf{x}_0$ and $\tilde{\mathbf{x}}_0$, and other perceptual losses[10] in VQGAN.

We highlight that, with this design, MS-VQGAN can not only encode the input image into multi-scale codes of different semantic levels but also preserve more structure and detail, as later analyzed in Section 4.3 of model ablation.

## 3.2   Feature Pyramid Latent Diffusion Model

After the MS-VQGAN is trained, we can use it to encode an image into multi-level feature maps $\mathcal{Z}$. Next, we introduce the feature Pyramid Diffusion Model (*Frido*) to model the underlying feature distribution and then generate images from noises. Similar to other DMs, *Frido* contains two parts: the *diffusion process* and the *denoising process*.

Diffusion Process of *Frido*   Instead of naively adding noises simultaneously on all N feature scales $\mathcal{Z} = \{\mathbf{z}^1, ..., \mathbf{z}^N\}$ at each of the T steps, we conduct diffusion process sequentially from low-level ($\mathbf{z}^1$) to high-level ($\mathbf{z}^N$), and each level takes T diffusion steps (total of $N \times T$ timesteps). See the top half of Figure 3b for an illustration.

Different from the classical diffusion process that corrupts pixels into noise in an unbiased way, we observe that *Frido*'s diffusion process starts from corrupting the object details, object shape, and finally the structure of the entire image. This allows *Frido* to capture information in different semantic levels. See Fig 1 for qualitative examples.

---

[5]θ denotes the learnable parameters, which is a U-Net (Ronneberger, Fischer, and Brox 2015) in Ho, Jain, and Abbeel (2020).

[6]Can be computed by interpolating $\mathbf{x}_0$ and ϵ with the weight schedule β_t. ϵ is sampled Gaussian noise.

[7]$\mathbf{z}_0 \in \mathcal{R}^{c \times h \times w}$, c is usually set to 4 and h, w are downsampled $8 - 16$ times from H, W

[8]$\tilde{\mathbf{z}}_0$ is sampled and denoised using Eq. (4).

[9]$\mathbf{z}^t \in \mathcal{R}^{c \times \frac{s}{2^{t-1}} \times \frac{s}{2^{t-1}}}$, N and c denotes the number of feature maps (stages) and the channel size of the feature, respectively; and s represents the size of the largest feature map.

[10]Patch discriminator loss and perceptual reconstruction loss.
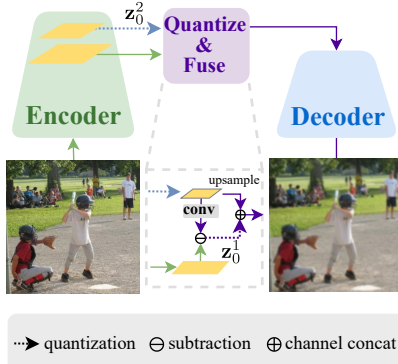
(a) Architecture of MS-VQGAN.
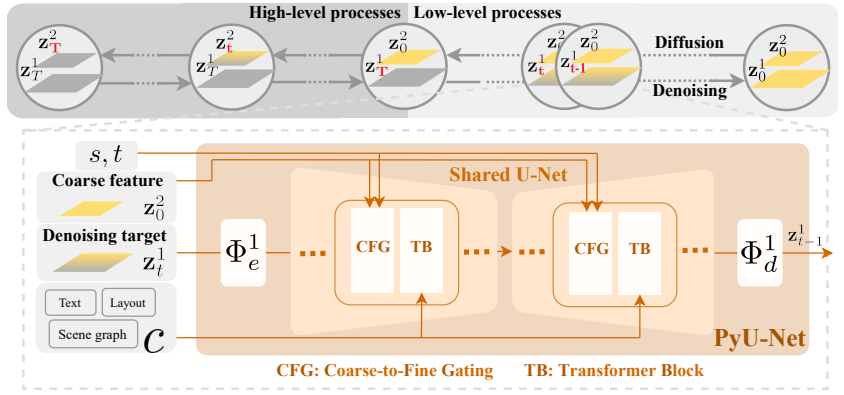
(b) Details of the diffusion and denoising processes.

Figure 3: Overview of *Frido* (best viewed in color). How MS-VQGAN encodes an image into multi-scale feature maps $\mathbf{z}_0^1, \mathbf{z}_0^2$ is illustrated in (a). The quantization enables VQ-VAE learning; and the fusion allows merging all representations from high to low level for the decoder to reconstruct an image. The upper half of (b) demonstrate the coarse-to-fine process, where the denoising is completed for high-level first, and then the lower one. The lower half of (b) details each denoising step. A U-Net is shared not only across timestep t but also the scale level s. Coarse-to-fine gating will be explained in Figure 4.

Denoising Process of *Frido* In the denoising phase, a sequence of neural function estimator $\epsilon_{\theta,t,n}$ is trained.[11] In order to denoise scale-by-scale, we introduce a novel feature pyramid U-Net (PyU-Net) as the neural approximator. PyU-Net can denoise the multi-scale features from high-level $\mathbf{z}^N$ to low-level $\mathbf{z}^1$ sequentially, achieving a coarse-to-fine generation. We highlight that, different from the LDMs, our PyU-Net is more suitable for coarse-to-fine diffusion with these two novel features: (1) *shared U-Net* with *lightweight level-specific layers* that project features of different levels to a shared space so that the heavier U-Net can be reused across all levels, reducing the trainable parameters, and (2) *coarse-to-fine gating* to condition the denoising of low-level features on high-level ones that are already generated.

Feature Pyramid U-Net The proposed PyU-Net learns the denoising process in a coarse-to-fine fashion. Take $N = 2$ ($\mathcal{Z} = \{\mathbf{z}_0^1, \mathbf{z}_0^2\}$) as an example (shown in Figure 3(b)), PyU-Net takes 4 inputs: (1) stage s and timestep t embeddings, (2) high-level feature conditions $\mathbf{z}_0^2$, (3) target feature map $\mathbf{z}_t^1$, and (4) other cross-modal conditions $\mathbf{c}$. By jointly observing these inputs, PyU-Net predicts the noise ϵ applied on the target feature $\mathbf{z}_t^1$, as shown in Figure 3b.

Instead of using a separate U-Net for each stage n, we opt for a single shared U-Net to reduce the parameter count. The input denoising target $\mathbf{z}_t^1$ is first projected by level-specific layers Φ_e^1 into a shared space so that a shared U-Net can be applied. Finally, another level-specific projection Φ_d^1 decodes the U-Net output to predict the noise ϵ added on $\mathbf{z}_t^1$, with the following objective similar to Eq. (3):

$$\mathcal{L}_{Frido} = \mathbb{E}_{z_0^n,\epsilon,t}\left[\|\epsilon - \epsilon_\theta(\mathbf{z}_t^n, \mathbf{z}_0^{n+1:N}, t)\|^2\right]. \quad (5)$$

We note that PyU-Net not only reduces the trainable parameters but also improves the results compared to vanilla per-stage U-Nets. For analysis, please refer to the experiments. Also, for training efficiency, we adopt the teacher
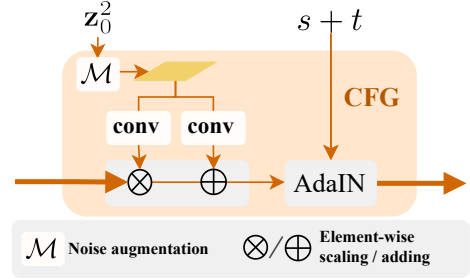

Figure 4: Framework of coarse-to-fine gating in PyU-Net.

forcing trick similar to sequence-to-sequence language models (Brown et al. 2020), where ground truth feature conditions are used while denoising the low-level map.

Coarse-to-Fine Gating *Frido* produces the latent codes sequentially from high-level to low-level feature maps. For example, while generating $\mathbf{z}_t^1$ (low-level), the model is conditioned on $\mathbf{z}_0^2$ (high-level). We, therefore, introduce a coarse-to-fine gating as shown in Figure 4.

Our coarse-to-fine gating (CFG) is designed with two major goals: 1) maintaining training efficiency with teacher forcing while preventing overfitting on ground truth, and 2) making the shared U-Net aware of the current stage and timestep. Thus, our CFG is composed of a feature noise augmentation and a spatial-temporal adaptive AdaIN (Park et al. 2019; Huang and Belongie 2017).

Specifically, given the high-level ground truth $\mathbf{z}_0^2$, we apply noise augmentation by $\mathcal{M}(\mathbf{z}_0^2)$, where $\mathcal{M}(\mathbf{z}_0^n) = \alpha \cdot \mathbf{z}_0^n + (1-\alpha) \cdot \epsilon$.[12] The input feature is then modulated by this augmented feature, with 2 convolutions, one for scaling and the other for shifting. Next, the output is passed to the spatial-temporal AdaIN, together with the summed embeddings of stage and timestep $s + t$, so that the shared U-Net is aware of the current spatial-temporal status.

To summarize, we highlight that our PyU-Net frame-

---

[11]$t = 1, 2, \ldots, T$ and $n = N, N-1, \ldots, 1$

[12]$\epsilon \sim \mathcal{N}(\mathbf{0}, \mathbf{I})$, and the scaler α is a hyper-parameter.

Methods	FID↓	IS↑	CLIP↑
Methods under standard T2I setting			
AttnGAN (Xu et al. 2018)	33.10	23.61	-
Obj-GAN (Li et al. 2019)	36.52	24.09	-
DM-GAN (Zhu et al. 2019)	27.34	**32.32**	-
DF-GAN (Tao et al. 2022)	21.42	-	-
LDM-8[†] (Rombach et al. 2022)	17.61	19.34	0.6500
VQ-diffusion[‡] (Gu et al. 2022)	14.06	21.85	0.6770
LDM-8-G[†]	12.27	27.86	0.6927
Frido-f16f8	15.38	19.32	0.6607
Frido-f16f8-G	**11.24**	26.82	**0.7046**
Methods with external pre-trained CLIP			
LAFITE-CLIP[‡] (Zhou et al. 2022)	**8.12**	32.24	0.7915
Frido-f16f8-G-CLIPr	8.97	27.43	**0.7991**

Table 1: Text-to-image generation on COCO. For LDM scores, $T = 250$; for *Frido*, $T = 200$. [†]: reproduced with official code and configs. [‡]: obtained from official model checkpoints. G: classifier-free guidance with scale $= 2.0$. Note that LAFITE used CLIP at training, while *Frido* uses it at inference only (CLIPr).

work equips DM with the ability to learn in a coarse-to-fine fashion with a moderate increase of parameters compared to classical hierarchical learning strategy (Razavi, Van den Oord, and Vinyals 2019). *Frido* inherits three generative paradigms, VAE, GAN, and DM, and is further embedded with a coarse-to-fine prior. Moreover, the diffusion operates on lower-resolution maps first, resulting a speedup at inference. Later, we show that SOTA results can be achieved under a similar compute budget to a strong, fast DM.

4 Experiments

In this section, we empirically demonstrate that *Frido* generates high-quality complex scene images that are also consistent to the multi-modal conditions, through the lens of text-to-image, scene-graph-to-image, and label-to-image generation tasks. Moreover, to emphasize the capability of capturing multiple objects in the images globally, we conduct experiments on layout-to-image generation. Lastly, extensive analyses are performed to validate design choices. We show that *Frido* achieved state-of-the-art FID scores on multiple tasks under 5 settings with improved inference speed.

Notations *Frido* can be trained with different feature resolutions and levels. For simplicity and readability, a latent feature map where each feature corresponding to $n \times n$ original image pixels is denoted fn. For example, a *Frido* to generate 256×256 images using 32×32 high-level and 64×64 low-level latent code is denoted *Frido*-f16f8. For LDM baselines, LDM-n encodes $n \times n$ pixels per feature.

4.1 Datasets and Evaluation

The main tasks we considered are text-to-image generation (T2I) on COCO (Lin et al. 2014), scene-graph-to-image generation (SG2I) on COCO-stuff and Visual Genome (VG) (Krishna et al. 2017), label-to-image generation (Label2I) (Jyothi et al. 2019) on COCO-stuff (Lin et al. 2014), and layout-to-image generation (Layout2I) on COCO-stuff and OpenImages (Kuznetsova et al. 2020). The

Methods	COCO			Visual Genome		
	FID↓	IS↑	CLIP↑	FID↓	IS↑	CLIP↑
GT	-	-	0.766	-	-	0.662
Sg2iIm	127.0	6.179	-	-	-	-
WSGC	119.1	7.235	-	45.7	10.69	-
LDMs-8[†]	49.14	13.33	0.627	36.88	14.60	0.611
Frido-f16f8	**46.11**	**13.41**	**0.642**	**31.61**	**15.07**	**0.613**

Table 2: Scene-graph-to-image generation on COCO and Visual Genome. [†]: reproduced with official code and configs.

standard metrics used to evaluate image synthesis tasks are Fréchet inception distance (FID) (Heusel et al. 2017) and Inception score (IS) (Salimans et al. 2016). In addition, we considered other task-specific metrics such as CLIP score (Hessel et al. 2021), Precision and Recall (Sajjadi et al. 2018), SceneFID (Sylvain et al. 2021), PSNR (Hore and Ziou 2010), and SSIM (Wang et al. 2004) when applicable. Please see the supplementary for detailed settings.[13]

4.2 Conditional Complex Scene Generation

Text Conditional Image Generation We first experiment on the standard text-to-image (T2I) generation for COCO, and the results are shown in Table 1.[14] In this setting, FID measures the image quality and CLIP-Score assesses the image-text consistency. For completeness, IS is also reported, though FID is known for a stronger correlation with human judgment than IS (Zhang et al. 2021; Sylvain et al. 2021). Besides standard diffusion inference, we also report the variant with classifier-free guidance (Nichol et al. 2022). As shown in Table 1, for both inference types, *Frido* significantly outperforms the previous best model LDM by $\approx$ 2 points for FID and $\approx$ 1 point for CLIP-Score, achieving state-of-the-art scores on FID (15.38 vs. 11.24) and CLIP-Score (0.6607 vs. 0.7046). In a different setting, LAFITE (Zhou et al. 2022) incorporated pre-trained CLIP (Radford et al. 2021), which contained abundant text-image knowledge from web-scale data pairs. As an initial step for incorporating CLIP knowledge with *Frido*, we report the results with a test-time only CLIP ranking trick (Ding et al. 2021) (10 inferences). We can see that CLIPr further improves all metrics significantly, achieving comparable FID and CLIP-Score to LAFITE. An orthogonal direction to utilize CLIP at training similar to LAFITE is left to future works.

Image Generation from Scene Graph To further verify the claimed semantic relation capturing, we run SG2I on COCO-stuff and VG datasets, and the results are shown in Table 2. Clearly, *Frido* outperforms all previous methods, including sg2im (Johnson, Gupta, and Li 2018), WSGC (Herzig et al. 2020), and LDMs, in terms of FID

---

[13]For completeness, we also experimented on unconditional image generation (UIG), including LSUN-bed (Yu et al. 2015), CelebA-HQ (Lee et al. 2020), and Lanscape (Skorokhodov, Sotnikov, and Elhoseiny 2021). Due to the page limit, please refer to the supplementary for UIG results and visual examples.

[14]We consider standard setting of training on COCO train2014 split. Orthogonal to recent T2I models pre-trained on huge image-text pairs, our goal is to synthesize images from diverse conditions.

Name	FID	IS	Precision	Recall
	3-8 labels in the image			
LayoutVAE	60.7	-	-	-
+LostGAN	74.06	11.66	0.231	0.473
LDMs-8[†]	51.45	**15.05**	0.434	0.576
Frido-f16f8	**47.39**	14.73	**0.437**	**0.595**
	2-30 labels in the image			
LDMs-8[†]	29.17	**18.00**	0.563	**0.554**
Frido-f16f8	**27.65**	17.70	**0.573**	0.542

Table 3: Label-to-image generation on COCO. [†]: reproduced with official code and configs.

Methods	COCO 256			OpenImage 256	
	FID↓	IS↑	SceneFID↓	FID↓	SceneFID↓
LostGAN-V2	42.55	-	-	-	-
OC-GAN	41.65	-	-	-	-
SPADE	41.11	-	-	-	-
VQGAN+T	56.58	-	24.07	45.33	15.85
LDM-8 (100 steps)	42.06	-	-	-	-
LDM-8[†] (100 steps)	41.02	17.01	21.63	-	-
LDM-4 (200 steps)	40.91	-	-	32.02	-
Frido-f16f8 (100 steps)	38.95	16.57	17.69	-	-
Frido-f8f4 (200 steps)	**37.14**	**18.62**	**14.91**	**29.04**	**12.77**

Table 4: Layout-to-image generation on COCO and Open-Images. [†]: reproduced with official code and configs.

and IS, achieving new state-of-the-art. Moreover, to quantitatively measure the semantic correctness of the image w.r.t. its SG condition, we transform the SG to captions by concatenating the relation triplets (i.e., subject-predicate-object) and report the CLIP-score of the resulting image-caption pairs. Our model surpasses previous work by $\approx 2\%$ on COCO and $\approx 0.2\%$ on VG. This empirically verifies that, with the feature pyramid and coarse-to-fine generation strategy, *Frido* improves modeling of complex relations.

Label-to-Image Generation Label-to-image produces scene image conditioned on image-level labels. Unlike T2I or SG2I, where scene structure is specified by the text conditions, this task requires a model to combine objects more freely and synthesize a coherent image. In addition to FID and IS, precision and recall are reported for object-level quality and diversity measurement, respectively. We conduct experiments on Label2I with COCO-stuff. As the shown in Table 3, our model outperforms all previous approaches, including LayoutVAE (Jyothi et al. 2019)[15] and LDMs, on not only FID but also precision and recall under the more common 3-8 labels setting. This indicates that, *Frido* achieves better image quality and data manifold modeling of multi-object images. We further challenge *Frido* with a harder 2-30 labels setting and still establish SOTA FID.

Layout-to-Image Generation Our Layout2I results show-cases that multiple objects' shapes and details can be synthesized. In Table 4, one can find that *Frido* outperforms previous methods, including LostGAN-v2 (Sun and Wu

---

[15]LayoutVAE implements Label2I as Label2Layout + Layout2I and reported 128 resolution result. We follow Yang et al. (2021) to adopt LostGAN (Sun and Wu 2019) to achieve 256 resolution.
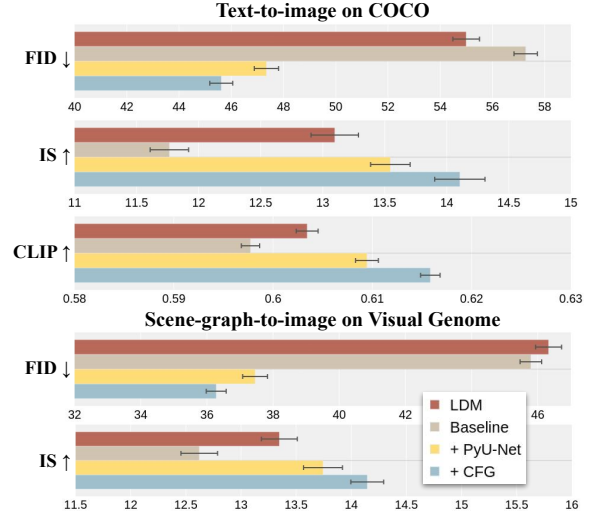

Figure 5: Model ablation on COCO T2I and VG SG2I. CFG denotes our coarse-to-fine gating.

2019), OC-GAN (Sylvain et al. 2021), SPADE (Park et al. 2019), VQGAN+T (combining Esser, Rombach, and Ommer 2021 and Brown et al. 2020), and LDM, on FID by at least 2 points, achieving new state-of-the-art for both COCO and OpenImages. Moreover, we achieve the best sceneFID, indicating the most visually realistic instance-level objects.

4.3 Model Analysis

Model Ablation To verify the key novel designs of *Frido*, we perform ablation studies on two tasks: text-to-image (T2I) on COCO and scene-graph-to-image (SG2I) on Visual Genome. Figure 5 showcases the contribution of each deployed component in *Frido*.[16] We report mean and the corresponding 95% confidence interval by conducting the bootstrap test (Koehn 2004).[17] For the baseline, we use two LDMs and perform a simple sequential learning strategy. More specifically, the first LDM learns the distribution of the high-level feature map (LDM-16); and the second LDM is deployed to model the low-level feature of f8 (LDM-8). In this baseline model, we concat LDM-8's output feature map and the denoising target feature feed into the LDM-8 for denoising. To justify the shared U-Net design of PyU-Net, we first apply this module without CFG to the baseline. Sharing U-Net reduces the model parameters from 1.18B (baseline) to 590M (baseline + PyU-Net). Finally, the coarse-to-fine gating is added, with only a minor increase in parameter count (total of 697M), and performance is further boosted for all metrics. We can see that each component significantly improves the generation results; models with PyU-Net and CFG are significantly better than the LDMs on all metrics.

Computation Cost Analysis Here we analyze the inference cost of our model. In Fig. 6, we compare *Frido* with

---

[16]For ablations and hyper-parameter tunings, we train for 250K iterations to allow more experiments. Models with the best dev scores are further trained to obtain the final test scores in Sec. 4.2.

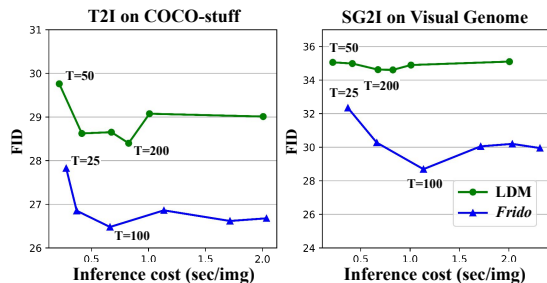[17]Sample size equals to test set size; resampled for 100 times.

Figure 6: Speed-quality trade-off analysis. Lower FID indicates better image quality.

Name	Scales	rFID	IS	PSNR	SSIM
VQGAN[†]	f8	5.51	28.98	43.56	0.9554
VQGAN-kl[†]	f8	5.02	**31.12**	42.94	0.9548
MS-VQGAN	f16f8	**4.67**	<u>29.31</u>	**44.77**	**0.9664**
MS-VQGAN	f32f16f8	6.68	27.67	44.40	0.9631

Table 5: Performance comparison of quantization models. These models are trained on OpenImage 256*256 images, and evaluated on COCO-stuff valid set. [†]: obtained from official model checkpoints.

LDM on the speed-quality trade-off. In this figure, we inference each model with different inference timesteps T and then plot the FID scores and against the per-image inference cost.[18] It is demonstrated that under similar inference budget, *Frido* achieve decent performance gain comparing to LDM, confirming the claimed efficiency of our model. For other comparisons on FLOPs, parameter counts, and inference time, please see the supplementary. Note that by operating in the latent space, LDM is among the faster ones within the DM model class. *Frido* further reduce the cost by putting part of the denoising load at lower-resolution.

MS-VQGAN Performance Vector quantization is the first stage of latent diffusion. Its performance may set the upper bound for the final generation quality. The purpose of the quantization model is to encode an image into low-dimensional and discrete space while being able to reconstruct the image. Therefore, we evaluate the reconstructed images of our MS-VQGAN in terms of reconstruction FID (rFID)[19], IS, PSNR, and SSIM to test the quantization performance. Also, we compare the results with the state-of-the-art quantization models, VQGAN and VQGAN-kl, and the results are shown in Table 5. For a fair comparison, the codebook sizes (vocabulary size $\times$ embedding dimension) for each setting is set equal. In Table 5, our MS-VQGAN outperforms previous methods on PSNR and SSIM, showing that our quantization model can better preserve visual details. Meanwhile, our method achieves comparable results on rFID and IS, demonstrating the image fidelity. Another observation is that keep increasing number of feature scales may not improve the performance, which will be further studied next.

---

[18]Done on validation splits with batch size of 32 using 1 V100.

[19]The FID score between the original images and the reconstructed ones.

Name	FID↓	IS↑	CLIP↑	Total Params	Inference time (1*V100) 32 BS
Frido-f32f16f8	48.04	12.45	0.567	788.9 M	1.227
Frido-f16f8f4	44.35	13.40	0.594	828.1 M	6.419
Frido-f16f8	40.14	14.25	**0.610**	697.8 M	0.918
Frido-f8f4	**38.68**	**14.38**	0.603	760.9 M	3.857

Table 6: Analysis of different feature scales on COCO T2I. The inference time is computed on a single V100 with 32 batch-size and 200 inference steps. Note that we compute the total parameters by summing parameters from MS-VQGAN, conditioning transformer, and *Frido*.
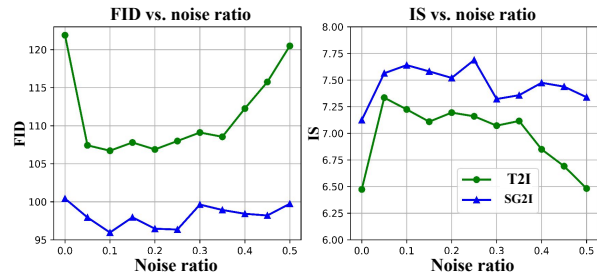

Figure 7: Analysis of noise augmentation.

Feature Scales of *Frido* We also analyze the performance of *Frido* with different feature scales (i.e., N in Section 3.2) by training *Frido* on COCO T2I. The results are reported in Table 6. For $N = 3$, we consider *Frido*-f32f16f8 and *Frido*-f16f8f4, and one can find that although the performance on all metrics is improved by using a higher resolution of features (i.e., *Frido*-f16f8f4), the parameter and inference cost also increase accordingly. This trade-off can also be seen in the $N = 2$ settings, where *Frido*-f8f4 boosts the FID from 40.14 to 38.68 while increasing the inference time by ≈ 4 times (since the resolution of f8f4 is also ≈ 4 times larger than f16f8). Moreover, by comparing *Frido*-f16f8 and *Frido*-f32f16f8, we notice that the performance decreases after adding a higher-level feature (i.e., f32). We hypothesize this is due to the weaker reconstruction ability of MS-VQGAN at f32f16f8 shown in Table 5. The increased FID indicates that adding the f32 layer does not help representing the original image in the quantized code, where the high-resolution codebook's capacity is reduced by 1/3. Moreover, *Frido* denoising starts from the f32 map, and the low quality of this denoised map results in error accumulation early in the coarse-to-fine generation, hence hurting the denoising at later stages. With the above observations, we adopt $N = 2$ (i.e., *Frido*-f16f8 and *Frido*-f8f4) for all of the tasks.

Noise Augmentation As mentioned in the CFG subsection in Methodology, we use ground truth higher-level feature maps in the training phase similar to teacher forcing in auto-regressive modelling. Without noise augmentation, the denoising process is prone to overfitting on such ground truth feature. We suspect this issue is caused by the train-test mismatch, where at inference, the denoising of f8 takes a *model-generated* f16 feature map as the input to the gating module. Therefore, the affected f8 feature output results in the lowered quality of visual details in the generated images. Here we study the effectiveness of the noise augmentation by analyzing different noise ratios α from 0.0 to 0.5.
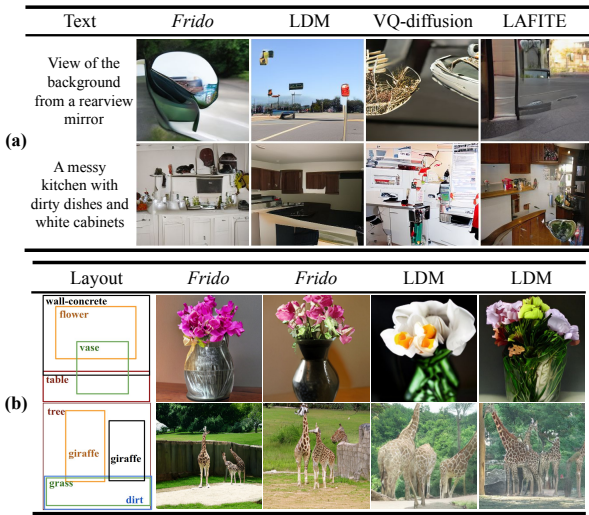
Figure 8: (a) Qualitative comparison on T2I. (b) Qualitative comparison on the Layout2I generation. Note that the layouts are obtained from the LDM paper (Rombach et al. 2022). Please see the supplementary for more tasks and examples.

The results are shown in Figure 7. We report the FID and IS scores of *Frido* on COCO T2I and VG SG2I. For simplicity, each setting is trained for 220k iterations with 32 batch sizes and evaluated on COCO 2017 validation set and VG validation set for T2I and SG2I, respectively. As shown in this figure, the performance of models without noise augmentation ($\alpha = 0$) increases from 106 to 122 on the FID score of the T2I task. On the other hand, the performance also drops when the noise ratio is set too high (e.g., $\alpha = 0.5$), because the higher-level feature may be too noisy to provide useful information for learning. By analyzing the trade-off, we choose $\alpha = 0.1$ as a default for *Frido*. As can be seen in Figure 7, this value is quite robust.

Takeaways The empirical studies have shown that *Frido* significantly outperforms the baseline LDM for complex scene image synthesis, and even achieves SOTA in 5 settings. Our modeling novelty, including PyU-Net and the coarse-to-fine gating, are statistically effective. Last but not least, *Frido* is more efficient, as can be seen in a head-to-head comparison to LDM, which mitigates the notorious heavy inference cost for diffusion models.

5 Related Work

More Generative Models for Image Synthesis The community has witnessed great progress of image synthesis in the past decade. Other than the previously discussed works, the families of GANs (Liao et al. 2022; Xu et al. 2018; Karras, Laine, and Aila 2019; Brock, Donahue, and Simonyan 2019; Gafni et al. 2022; Zhang et al. 2021; Hinz, Heinrich, and Wermter 2020), VAEs (Sohn, Lee, and Yan 2015), autoregressive models (Razavi, Van den Oord, and Vinyals 2019; Chang et al. 2022; Yu et al. 2022), flow-based methods (Dinh, Sohl-Dickstein, and Bengio 2017), and diffusion-based models (Saharia et al. 2022; Gu et al.

2022) have all made great contribution to shape this field. *Frido* is a hybrid of the VAE and DM family, combining the best of both worlds for outstanding image quality on complex scenes, and significantly improved DM inference. Very recently, large-scale pre-training for text-to-image generation (Ramesh et al. 2022) has gained vast attention and achieved superior results. *Frido* is orthogonal to these models, as we investigate coarse-to-fine synthesis and multi-modality inputs beyond text.

Two-Stage Generative Models Recently, many two-stage generative models (Van Oord, Kalchbrenner, and Kavukcuoglu 2016; Jahn, Rombach, and Ommer 2021; Pandey et al. 2022; Zhou et al. 2022) are proposed to tackle the drawbacks of the one-stage models. The representative VQ-VAE (Van Den Oord, Vinyals et al. 2017) first encodes an image into a discrete latent space with a lower spatial resolution and then uses an auto-regressive network to model such space. The first step is called Vector Quantization (VQ), which reduces the input information to allow auto-encoder learning. In addition, VQ bridges images to other modalities, such as language (Ding et al. 2021; Chen et al. 2020) and audio (Yan et al. 2021), seamlessly by converting to discrete tokens. In the second stage, an auto-regressive(e.g. PixelCNN (Van den Oord et al. 2016), VQGAN) or diffusion model (LDM, VQ-Diffusion (Tang et al. 2022)) is adopted to model the encoded latent space. *Frido* contributes to both stages by proposing MS-VQGAN and PyU-Net for DM.

Coarse-to-Fine Image Generation Approaches Instead of generating a full-resolution image in one step, coarse-to-fine generation synthesizes an image with multiple steps, from low to high resolution in pixel space (Gregor et al. 2015; Mansimov et al. 2016; Ho et al. 2022) or from high-level to low-level information in latent space (Razavi, Van den Oord, and Vinyals 2019; Child et al. 2019). These allow model to better capture the information in different levels and have shown to achieve higher quality. For instance, AttnGAN (Xu et al. 2018) and StackGAN (Zhang et al. 2017, 2018) first produce an image in low resolution (e.g., 1/8 of the full-size) and then iteratively scale up the generated image until achieving the final resolution. Different from the above works, we share the core network for each scale. Therefore, the overhead compared to single-scale models is minimized.

6 Conclusion

We propose *Frido*, a new image generative model, empowering an under-explored coarse-to-fine prior in the diffusion model family. Key designs such as multi-scale codebooks, a single shared U-Net, and the special gating mechanism are shown to be effective via extensive experiments. Empirically, we apply this model to a diverse set of cross-modal image synthesis tasks and achieve 5 new state-of-the-art results. From a practical aspect, *Frido* also mitigates the well-known slow inference pain-point of diffusion methods.

7 Acknowledgement

References

Anokhin, I.; Demochkin, K.; Khakhulin, T.; Sterkin, G.; Lempitsky, V.; and Korzhenkov, D. 2021. Image generators with conditionally-independent pixel synthesis. In *CVPR*.

Brock, A.; Donahue, J.; and Simonyan, K. 2019. Large scale GAN training for high fidelity natural image synthesis. In *ICLR*.

Brown, T.; Mann, B.; Ryder, N.; Subbiah, M.; Kaplan, J. D.; Dhariwal, P.; Neelakantan, A.; Shyam, P.; Sastry, G.; Askell, A.; et al. 2020. Language models are few-shot learners. In *NeurIPS*.

Brundage, M.; Avin, S.; Clark, J.; Toner, H.; Eckersley, P.; Garfinkel, B.; Dafoe, A.; Scharre, P.; Zeitzoff, T.; Filar, B.; et al. 2018. The malicious use of artificial intelligence: Forecasting, prevention, and mitigation. *arXiv preprint arXiv:1802.07228*.

Casanova, A.; Careil, M.; Verbeek, J.; Drozdzal, M.; and Romero Soriano, A. 2021. Instance-conditioned gan. In *NeurIPS*.

Chang, H.; Zhang, H.; Jiang, L.; Liu, C.; and Freeman, W. T. 2022. Maskgit: Masked generative image transformer. In *CVPR*.

Chen, M.; Radford, A.; Child, R.; Wu, J.; Jun, H.; Luan, D.; and Sutskever, I. 2020. Generative pretraining from pixels. In *ICML*.

Child, R.; Gray, S.; Radford, A.; and Sutskever, I. 2019. Generating long sequences with sparse transformers. *arXiv preprint arXiv:1904.10509*.

Devlin, J.; Chang, M.-W.; Lee, K.; and Toutanova, K. 2019. Bert: Pre-training of deep bidirectional transformers for language understanding. In *NAACL-HLT*.

Dhariwal, P.; and Nichol, A. 2021. Diffusion models beat gans on image synthesis. In *NeurIPS*.

Ding, M.; Yang, Z.; Hong, W.; Zheng, W.; Zhou, C.; Yin, D.; Lin, J.; Zou, X.; Shao, Z.; Yang, H.; et al. 2021. Cogview: Mastering text-to-image generation via transformers. In *NeurIPS*.

Dinh, L.; Krueger, D.; and Bengio, Y. 2014. Nice: Nonlinear independent components estimation. *arXiv preprint arXiv:1410.8516*.

Dinh, L.; Sohl-Dickstein, J.; and Bengio, S. 2017. Density estimation using real nvp. In *ICLR*.

Esser, P.; Rombach, R.; Blattmann, A.; and Ommer, B. 2021. Imagebart: Bidirectional context with multinomial diffusion for autoregressive image synthesis. In *NeurIPS*.

Esser, P.; Rombach, R.; and Ommer, B. 2021. Taming transformers for high-resolution image synthesis. In *CVPR*.

Falcon, W.; and team, T. P. L. 2019. PyTorch Lightning. *https://www.pytorchlightning.ai*.

Gafni, O.; Polyak, A.; Ashual, O.; Sheynin, S.; Parikh, D.; and Taigman, Y. 2022. Make-a-scene: Scene-based text-to-image generation with human priors. *arXiv preprint arXiv:2203.13131*.

Goodfellow, I.; Pouget-Abadie, J.; Mirza, M.; Xu, B.; Warde-Farley, D.; Ozair, S.; Courville, A.; and Bengio, Y. 2014. Generative adversarial nets. In *NeurIPS*.

Gregor, K.; Danihelka, I.; Graves, A.; Rezende, D.; and Wierstra, D. 2015. Draw: A recurrent neural network for image generation. In *ICML*.

Gu, S.; Chen, D.; Bao, J.; Wen, F.; Zhang, B.; Chen, D.; Yuan, L.; and Guo, B. 2022. Vector quantized diffusion model for text-to-image synthesis. In *CVPR*.

Herzig, R.; Bar, A.; Xu, H.; Chechik, G.; Darrell, T.; and Globerson, A. 2020. Learning canonical representations for scene graph to image generation. In *ECCV*.

Hessel, J.; Holtzman, A.; Forbes, M.; Bras, R. L.; and Choi, Y. 2021. Clipscore: A reference-free evaluation metric for image captioning. In *EMNLP*.

Heusel, M.; Ramsauer, H.; Unterthiner, T.; Nessler, B.; and Hochreiter, S. 2017. Gans trained by a two time-scale update rule converge to a local nash equilibrium. In *NeurIPS*.

Hinz, T.; Heinrich, S.; and Wermter, S. 2020. Semantic object accuracy for generative text-to-image synthesis. *TPAMI*.

Ho, J.; Jain, A.; and Abbeel, P. 2020. Denoising diffusion probabilistic models. In *NeurIPS*.

Ho, J.; Saharia, C.; Chan, W.; Fleet, D. J.; Norouzi, M.; and Salimans, T. 2022. Cascaded Diffusion Models for High Fidelity Image Generation. *JMLR*.

Hore, A.; and Ziou, D. 2010. Image quality metrics: PSNR vs. SSIM. In *ICPR*.

Huang, X.; and Belongie, S. 2017. Arbitrary style transfer in real-time with adaptive instance normalization. In *ICCV*.

Jahn, M.; Rombach, R.; and Ommer, B. 2021. High-Resolution Complex Scene Synthesis with Transformers. *arXiv preprint arXiv:2105.06458*.

Johnson, J.; Gupta, A.; and Li, F.-F. 2018. Image generation from scene graphs. In *CVPR*.

Jyothi, A. A.; Durand, T.; He, J.; Sigal, L.; and Mori, G. 2019. Layoutvae: Stochastic scene layout generation from a label set. In *ICCV*.

Karras, T.; Aila, T.; Laine, S.; and Lehtinen, J. 2017. Progressive growing of gans for improved quality, stability, and variation. *arXiv preprint arXiv:1710.10196*.

Karras, T.; Laine, S.; and Aila, T. 2019. A style-based generator architecture for generative adversarial networks. In *CVPR*.

Karras, T.; Laine, S.; Aittala, M.; Hellsten, J.; Lehtinen, J.; and Aila, T. 2020. Analyzing and improving the image quality of stylegan. In *CVPR*.

Kim, D.; Shin, S.; Song, K.; Kang, W.; and Moon, I.-C. 2022. Soft truncation: A universal training technique of score-based diffusion model for high precision score estimation. In *ICML*.

Kingma, D. P.; and Dhariwal, P. 2018. Glow: Generative flow with invertible 1x1 convolutions. In *NeurIPS*.

Kingma, D. P.; and Welling, M. 2014. Auto-encoding variational bayes. In *ICLR*.

Koehn, P. 2004. Statistical significance tests for machine translation evaluation. In *EMNLP*.

Krishna, R.; Zhu, Y.; Groth, O.; Johnson, J.; Hata, K.; Kravitz, J.; Chen, S.; Kalantidis, Y.; Li, L.-J.; Shamma, D. A.; et al. 2017. Visual genome: Connecting language and vision using crowdsourced dense image annotations. *IJCV*.

Kuznetsova, A.; Rom, H.; Alldrin, N.; Uijlings, J.; Krasin, I.; Pont-Tuset, J.; Kamali, S.; Popov, S.; Malloci, M.; Kolesnikov, A.; et al. 2020. The open images dataset v4. *IJCV*.

Kynkäänniemi, T.; Karras, T.; Laine, S.; Lehtinen, J.; and Aila, T. 2019. Improved precision and recall metric for assessing generative models. In *NeurIPS*.

Lee, C.-H.; Liu, Z.; Wu, L.; and Luo, P. 2020. MaskGAN: Towards Diverse and Interactive Facial Image Manipulation. In *CVPR*.

Li, W.; Zhang, P.; Zhang, L.; Huang, Q.; He, X.; Lyu, S.; and Gao, J. 2019. Object-driven text-to-image synthesis via adversarial training. In *CVPR*.

Liao, W.; Hu, K.; Yang, M. Y.; and Rosenhahn, B. 2022. Text to image generation with semantic-spatial aware GAN. In *CVPR*.

Lin, T.-Y.; Maire, M.; Belongie, S.; Hays, J.; Perona, P.; Ramanan, D.; Dollár, P.; and Zitnick, C. L. 2014. Microsoft coco: Common objects in context. In *ECCV*.

Mansimov, E.; Parisotto, E.; Ba, J. L.; and Salakhutdinov, R. 2016. Generating images from captions with attention. In *ICLR*.

Nichol, A.; Dhariwal, P.; Ramesh, A.; Shyam, P.; Mishkin, P.; McGrew, B.; Sutskever, I.; and Chen, M. 2022. Glide: Towards photorealistic image generation and editing with text-guided diffusion models. In *ICML*.

Nichol, A. Q.; and Dhariwal, P. 2021. Improved denoising diffusion probabilistic models. In *ICML*.

Pandey, K.; Mukherjee, A.; Rai, P.; and Kumar, A. 2022. DiffuseVAE: Efficient, Controllable and High-Fidelity Generation from Low-Dimensional Latents. *arXiv preprint arXiv:2201.00308*.

Park, T.; Liu, M.-Y.; Wang, T.-C.; and Zhu, J.-Y. 2019. Semantic image synthesis with spatially-adaptive normalization. In *CVPR*.

Parmar, G.; Li, D.; Lee, K.; and Tu, Z. 2021. Dual contradistinctive generative autoencoder. In *CVPR*.

Radford, A.; Kim, J. W.; Hallacy, C.; Ramesh, A.; Goh, G.; Agarwal, S.; Sastry, G.; Askell, A.; Mishkin, P.; Clark, J.; et al. 2021. Learning transferable visual models from natural language supervision. In *ICML*.

Radford, A.; Metz, L.; and Chintala, S. 2015. Unsupervised representation learning with deep convolutional generative adversarial networks. *arXiv preprint arXiv:1511.06434*.

Ramesh, A.; Dhariwal, P.; Nichol, A.; Chu, C.; and Chen, M. 2022. Hierarchical text-conditional image generation with clip latents. *arXiv preprint arXiv:2204.06125*.

Razavi, A.; Van den Oord, A.; and Vinyals, O. 2019. Generating diverse high-fidelity images with vq-vae-2. In *NeurIPS*.

Rombach, R.; Blattmann, A.; Lorenz, D.; Esser, P.; and Ommer, B. 2022. High-resolution image synthesis with latent diffusion models. In *CVPR*.

Ronneberger, O.; Fischer, P.; and Brox, T. 2015. U-net: Convolutional networks for biomedical image segmentation. In *MICCAI*.

Saharia, C.; Chan, W.; Saxena, S.; Li, L.; Whang, J.; Denton, E.; Ghasemipour, S. K. S.; Ayan, B. K.; Mahdavi, S. S.; Lopes, R. G.; et al. 2022. Photorealistic Text-to-Image Diffusion Models with Deep Language Understanding. *arXiv preprint arXiv:2205.11487*.

Sajjadi, M. S.; Bachem, O.; Lucic, M.; Bousquet, O.; and Gelly, S. 2018. Assessing generative models via precision and recall. In *NeurIPS*.

Salimans, T.; Goodfellow, I.; Zaremba, W.; Cheung, V.; Radford, A.; and Chen, X. 2016. Improved techniques for training gans. In *NeurIPS*.

Sauer, A.; Chitta, K.; Müller, J.; and Geiger, A. 2021. Projected gans converge faster. In *NeurIPS*.

Skorokhodov, I.; Sotnikov, G.; and Elhoseiny, M. 2021. Aligning latent and image spaces to connect the unconnectable. In *ICCV*.

Sohl-Dickstein, J.; Weiss, E.; Maheswaranathan, N.; and Ganguli, S. 2015. Deep unsupervised learning using nonequilibrium thermodynamics. In *ICML*.

Sohn, K.; Lee, H.; and Yan, X. 2015. Learning structured output representation using deep conditional generative models. In *NeurIPS*.

Sun, W.; and Wu, T. 2019. Image synthesis from reconfigurable layout and style. In *ICCV*.

Sylvain, T.; Zhang, P.; Bengio, Y.; Hjelm, R. D.; and Sharma, S. 2021. Object-centric image generation from layouts. In *AAAI*.

Tan, S.; Shen, Y.; and Zhou, B. 2020. Improving the fairness of deep generative models without retraining. *arXiv preprint arXiv:2012.04842*.

Tang, Z.; Gu, S.; Bao, J.; Chen, D.; and Wen, F. 2022. Improved Vector Quantized Diffusion Models. *arXiv preprint arXiv:2205.16007*.

Tao, M.; Tang, H.; Wu, F.; Jing, X.-Y.; Bao, B.-K.; and Xu, C. 2022. DF-GAN: A Simple and Effective Baseline for Text-to-Image Synthesis. In *CVPR*.

Vahdat, A.; Kreis, K.; and Kautz, J. 2021. Score-based generative modeling in latent space. In *NeurIPS*.

Van den Oord, A.; Kalchbrenner, N.; Espeholt, L.; Vinyals, O.; Graves, A.; et al. 2016. Conditional image generation with pixelcnn decoders. In *NeurIPS*.

Van Den Oord, A.; Vinyals, O.; et al. 2017. Neural discrete representation learning. In *NeurIPS*.

Van Oord, A.; Kalchbrenner, N.; and Kavukcuoglu, K. 2016. Pixel recurrent neural networks. In *ICML*.

Wang, Z.; Bovik, A. C.; Sheikh, H. R.; and Simoncelli, E. P. 2004. Image quality assessment: from error visibility to structural similarity. *TIP*.

Xu, T.; Zhang, P.; Huang, Q.; Zhang, H.; Gan, Z.; Huang, X.; and He, X. 2018. Attngan: Fine-grained text to image generation with attentional generative adversarial networks. In *CVPR*.

Yan, W.; Zhang, Y.; Abbeel, P.; and Srinivas, A. 2021. Videogpt: Video generation using vq-vae and transformers. *arXiv preprint arXiv:2104.10157*.

Yang, C.-F.; Fan, W.-C.; Yang, F.-E.; and Wang, Y.-C. F. 2021. Layouttransformer: Scene layout generation with conceptual and spatial diversity. In *CVPR*.

Yu, F.; Seff, A.; Zhang, Y.; Song, S.; Funkhouser, T.; and Xiao, J. 2015. Lsun: Construction of a large-scale image dataset using deep learning with humans in the loop. *arXiv preprint arXiv:1506.03365*.

Yu, J.; Li, X.; Koh, J. Y.; Zhang, H.; Pang, R.; Qin, J.; Ku, A.; Xu, Y.; Baldridge, J.; and Wu, Y. 2022. Vector-quantized image modeling with improved vqgan. In *ICML*.

Zhang, H.; Koh, J. Y.; Baldridge, J.; Lee, H.; and Yang, Y. 2021. Cross-modal contrastive learning for text-to-image generation. In *CVPR*.

Zhang, H.; Xu, T.; Li, H.; Zhang, S.; Wang, X.; Huang, X.; and Metaxas, D. N. 2017. Stackgan: Text to photo-realistic image synthesis with stacked generative adversarial networks. In *ICCV*.

Zhang, H.; Xu, T.; Li, H.; Zhang, S.; Wang, X.; Huang, X.; and Metaxas, D. N. 2018. Stackgan++: Realistic image synthesis with stacked generative adversarial networks. *TPAMI*.

Zhou, Y.; Zhang, R.; Chen, C.; Li, C.; Tensmeyer, C.; Yu, T.; Gu, J.; Xu, J.; and Sun, T. 2022. LAFITE: Towards Language-Free Training for Text-to-Image Generation. In *CVPR*.

Zhu, M.; Pan, P.; Chen, W.; and Yang, Y. 2019. Dm-gan: Dynamic memory generative adversarial networks for text-to-image synthesis. In *CVPR*.

A   Diffusion and Denoising Details

A.1   Formulation of the Diffusion and Denoising Process of *Frido*

With the deployment of the MS-VQGAN mentioned in Section 3.1, *Frido* is able to encode the input image into feature maps $\mathcal{Z}$ with different spatial levels. We then introduce feature pyramid diffusion model (*Frido*) to further learn the distribution of the latent space and generate images from sampled normal distribution variables. Similar to other diffusion methods (DMs), our *Frido* contains two parts: the *diffusion process* and the *denoising process*. We now detail these two parts in the following paragraphs.

Diffusion Process of *Frido*   The diffusion process aims at producing the approximate posterior $q(\mathbf{Z}_{1:T}|\mathbf{z}_0)$, which is fixed to a Markov chain that gradually adds Gaussian noise to the input data based on a fixed schedule $\beta_1, ..., \beta_T$. As shown in Figure 3, instead of directly adding noise on the multi-scale feature maps $\mathcal{Z} = \{\mathbf{z}^1, \mathbf{z}^2, ..., \mathbf{z}^N\}$, we conduct diffusion process on each scale of feature map sequentially from low-level one (i.e., $\mathbf{z}^1$) to high-level one (i.e., $\mathbf{z}^N$) over the course of N × T timesteps. That is, the approximate posterior q can be formulated as follows.

$$q(\mathbf{z}_{1:T}^{1:N}|\mathcal{Z}) = \prod_{n=1}^{N}\prod_{t=1}^{T} q(\mathbf{z}_t^n|\mathbf{z}_{t-1}^n), \text{ and} \tag{6}$$
$$q(\mathbf{z}_t^n|\mathbf{z}_{t-1}^n) = \mathcal{N}(\sqrt{1-\beta_t}\mathbf{z}_{t-1}^n, \beta_t\mathbf{I}),$$

where noise schedules β can be fixed or learnable parameters. Different from the classical diffusion process that corrupts pixels into noise in an unbiased way, we observe that *Frido* 's diffusion process starts from corrupting the object details, object shape, and finally the structure of the entire image. This allows Frido to capture information in different semantic levels.

Denoising Process of *Frido*   The denoising process starts from the joint distribution $p(\mathbf{z}_T^{1:N}) \sim \mathcal{N}(\mathbf{z}_T^{1:N}; \mathbf{0}, \mathbf{I})$. That is, feature maps of all scales are initialized from a normal distribution. Different from classical denoising process as Eq. 2, we conduct the denoising process from high-level feature maps $p(\mathbf{z}_T^N)$ to low-level feature map $p(\mathbf{z}_T^1)$ sequentially, achieving coarse-to-fine generation. In other words, the denoising process for n-th scale would be based on the previous produced feature maps $\mathbf{z}_0^N, \mathbf{z}_0^{N-1}, ..., \mathbf{z}_0^{n+1}$ and can be formulated as $p_\theta(\mathbf{z}_0^n|\mathbf{z}_0^{n+1:N}) = \int p_\theta(\mathbf{z}_{0:T}^n|\mathbf{z}^{n+1:N})d\mathbf{z}_{1:T}^n$, where

$$p_\theta(\mathbf{z}_{0:T}^n|\mathbf{z}^{n+1:N}) = p(\mathbf{z}_T^n)\prod_{t=1}^{T} p_\theta(\mathbf{z}_{t-1}^n|\mathbf{z}_t^n, \mathbf{z}^{n+1:N}), \text{ and}$$
$$p_\theta(\mathbf{z}_{t-1}|\mathbf{z}_t, \mathbf{z}^{n+1:N}) =$$
$$\mathcal{N}(\mathbf{z}_{t-1}; \mu_\theta(\mathbf{z}_t, t, \mathbf{z}^{n+1:N}), \sigma_\theta(\mathbf{z_t}, t, \mathbf{z}^{n+1:N})). \tag{7}$$

Practically, a designed denoising autoencoder ϵ_θ is adopted to we can simplify our model as a sequence of

denoising autoencoder $\epsilon_\theta(\mathbf{z}_t^n, \mathbf{z}_0^{n+1:N}, t)$, $t = 1...T$ and $n = N...1$, with the goal of predicting the added noise variant on the $\mathbf{z}_t^n$. We then adopt our feature pyramid U-Net (PyU-Net) as the denoising autoencoder ϵ_θ and the objective function can be formulated as follows. (modified from Eq.3)

$$\mathcal{L}_{Frido} =$$
$$\mathbb{E}_{\mathbf{z}_0^n,\epsilon,t}\left[\|\epsilon - \epsilon_\theta(\sqrt{\tilde{\alpha}_t}\mathbf{z}_0^n + \sqrt{1-\tilde{\alpha}_t}\epsilon, \mathbf{z}_0^{n+1:N})\|^2\right], \tag{8}$$

where t is uniformly sampled from 1, . . . , T, and n is uniformly sampled from 1, . . . , N. In the testing phase, the samples from $p(\mathbf{z}_0^{1:N})$ can be decoded back to image pixel space with the pre-trained decoder $\mathcal{D}$.

B   Implementation Details

For the reproducibility of *Frido*, we detail the implementation details for each task, including but not limit to the training/testing environment, hyper-parameters setting for each task, and the details of encoding multi-modal conditions.

B.1   Training/Testing Environment

In this paper, if not specified, models are trained on a Linux environment with 8 Nvidia Tesla V100. Also, the training and testing are powered by Pytorch Lightning (Falcon and team 2019) of 1.4.2, with operational precision as float32. While training, models are run with raw batch size on each GPU without the gradient accumulation trick. For better reproducibility, we use the "*seed_everything*" tools in Pytorch Lightning to fix the random seeds in the training phase with seed=23. For the optimization setting, we use the AdamW algorithm as the optimizer with the default setting as follows: betas= $(0.9, 0.999)$, eps= $1e - 08$, weight decay= 0.01, and learning rates are specified in the later hyper-parameters setting section. A learning rate scheduler is not used in the training of our methods, if not specified.

B.2   Hyper-Parameter Settings

For a better understanding of the hyper-parameter setting of *Frido* for each task, we provide an overview of hyper-parameter settings of all *Frido* models in this paper. For conditional image generation tasks, the hyper-parameter settings are listed in Table A. For unconditional image generation, we detail the settings in Table B. As for modal analysis, the settings of the hyper-parameter are provided in Table C.

B.3   Encoding Multi-Modal Conditions

Text-to-image Generation   Similar to previous diffusion works (Rombach et al. 2022; Nichol et al. 2022), we use BERT Embedder to convert a sequence of text conditions into a sequence of embeddings. Specifically, given a caption as a cross-modal condition, a BERT tokenizer is deployed to tokenize a caption into a sequence of tokens, followed by a BERT transformer module to encode these tokens to a sequence of embeddings.
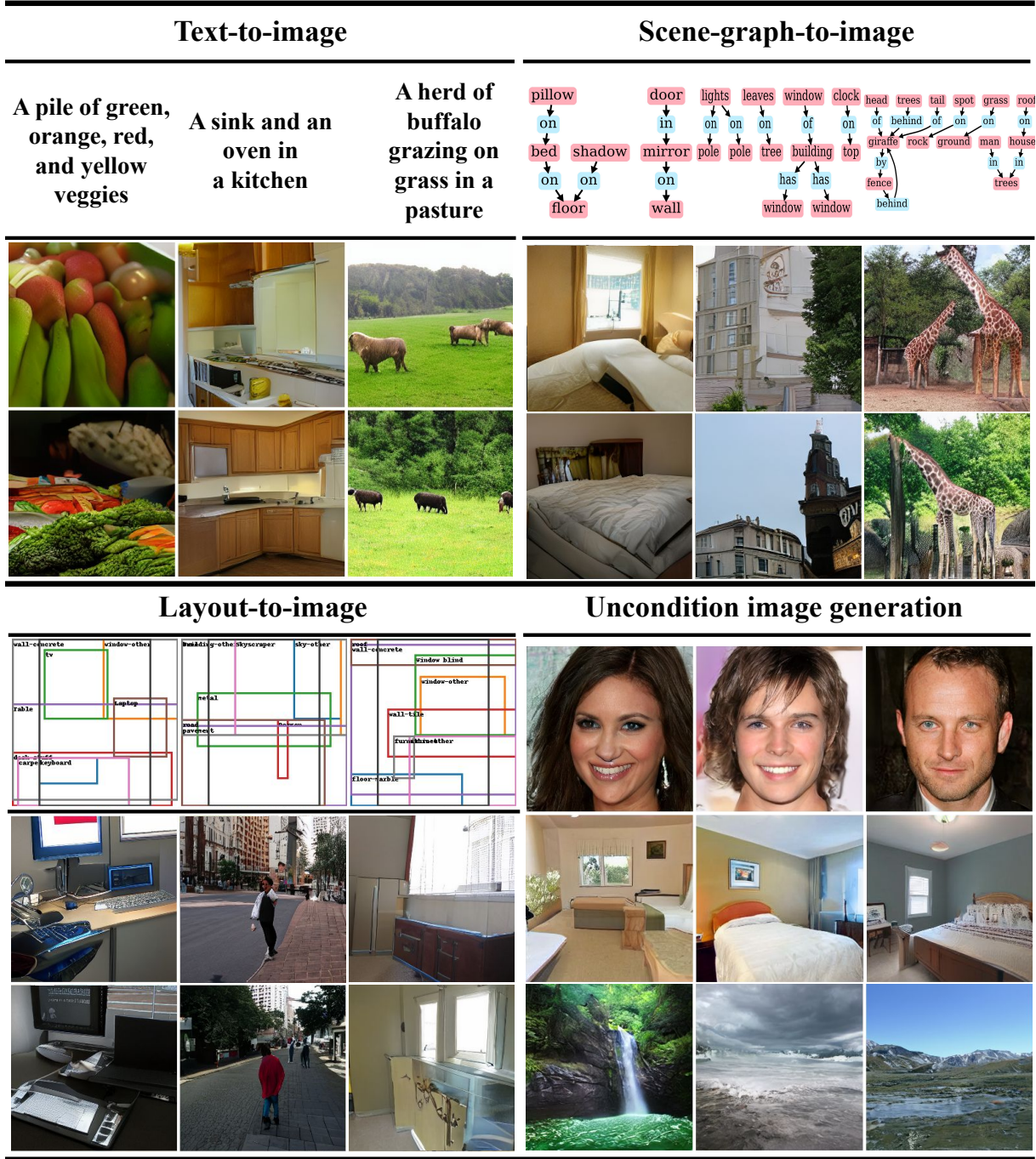
Figure A: Generated examples of *Frido* on various tasks. Full-scale version of Fig. 2 in the main paper.

Image Generation from Scene Graph Similar to LT-Net (Yang et al. 2021), we first transform the scene graph conditions into three sequences of tokens, including the *word tokens*, *part-of-pair tokens* (Yang et al. 2021), and *object ID* tokens. After that, the final condition embedding sequence can be obtained by first adopting BERT-tokenizer (Devlin et al. 2019) to encode these tokens into embeddings and sum up these embeddings.

Layout-to-Image Generation To encode a sequence of image-level labels into an embedding sequence, we first map the labels to the corresponding category names. After that, these class names are concatenated as a text sequence and encoded by a similar encoding approach used in text-to-image generation.

Layout-to-Image Generation We follow the layout discretization process in LDM (Rombach et al. 2022) to trans-

Hyper-parameter	T2I (Frido-f16f8)	SG2I (Frido-f16f8)	Label2I (Frido-f16f8)	Layout2I (Frido-f16f8)	Layout-to-image (Frido-f8f4)
General settings					
Base learning rate	2e-7	2e-7	1e-6	2e-7	1e-7
Scale lr	True	True	False	True	True
Batch size	32	32	32	32	12
Training epochs	300	250/150 (COCO/VG)	150	500	200/25 (COCO/IO)
MS-VQGAN	MS-VQGAN-f16f8	MS-VQGAN-f16f8	MS-VQGAN-f16f8	MS-VQGAN-f16f8	MS-VQGAN-f8f4
Diffusion steps	1000	1000	1000	1000	1000
Noise Schedule	linear	linear	linear	linear	linear
Number of feature scales	2	2	2	2	2
PyU-Net settings					
Model channels	192	192	192	192	192
Number of res blocks	2	2	2	2	2
Attention resolutions	2, 4, 8	2, 4, 8	2, 4, 8	2, 4, 8	2, 4, 8
Channel multiplier	1, 2, 3, 5	1, 2, 3, 5	1, 2, 3, 5	1, 2, 3, 5	1, 2, 3, 5
Transformer depth	1	1	1	1	1
Number of heads	6	6	6	6	6
Context dim	640	640	640	640	640
Noise ratio	0.1	0.1	0.1	0.1	0.1
Multi-modal Condition Encoding settings					
Encoding module	BERTEmbedder	BERTEmbedder	BERTEmbedder	BERTEmbedder	BERTEmbedder
Number of layer	32	32	32	32	32
Attention embedding dim	640	640	640	640	640
Vocab size	30522	30522	30522	30522	30522
Max sequence length	77	180	77	96	96

Table A: Hyper-parameter settings for all *Frido* of all conditional tasks, including text-to-image (T2I), scene-graph-to-image (SG2I), label-to-image (Label2I), and layout-to-image (Layout2I) in this paper. IO denotes Open-Image dataset. If model converges earlier, we used the checkpoint with best total ema loss. Note that, for *Frido*-f8f4 on COCO, model was fine-tuned from the one trained on OI.

form the layout of an image into a sequence of tokens, where conditions are discretized into multiple triples. Each triple represents the spatial locations, size, and category of the corresponding bounding box. More specifically, each bounding box is encoded as a (l, b, c)-tuple, where l denotes the top-left and b the bottom-right position. c represents the category of the bounding box. With a sequence of tokens obtained, we adopt a BERT transformer encoder to encode the sequence.

C Datasets and Evaluations

C.1 Evaluation Metrics

For quantitative experiments, we consider various metrics from different aspects to evaluate our method on each task. We now introduce these metrics as follows:

- To measure the image quality, we consider Fréchet inception distance (FID) and Inception score (IS). IS evaluates the distribution of generated images by an Inception-V3 model pre-trained on ImageNet. Unlike the inception score, FID takes the real image used to train the generative model into consideration and compares the distribution of that with the distribution of generated images, making it a widely-used metric to access the image quality. Practically, we use *torch-fidelity*[20] to calculate the FID and inception score. Furthermore, sceneFID (Sylvain et al. 2021) is considered to measure the image quality at instance-level. To calculate SceneFID, we follow Sylvain et al. (2021) to first crop the generated images by the corresponding ground truth bounding boxes, yielding the generated instances. After that, similar to FID score, we use *torch-fidelity* to calculate the FID score between ground truth instances and the generated instances.

- In order to perform the quantitative analysis on the semantic correctness of text-to-image or scene-graph-to-image generation, we take into account of reference-free CLIP score (CLIPscore) (Hessel et al. 2021) as the measurement for these tasks. CLIPsocre adopt CLIP (Radford et al. 2021) pre-trained on 400M image-caption pairs from the web dataset to assess image-caption compatibility. In this paper, we use the officially released code[21] to calculate the CLIP score.

- Precision and Recall for image generation task (Sajjadi et al. 2018; Kynkäänniemi et al. 2019) is to measure the distribution coverage of a trained generative model. In other words, precision is the probability that a sample from a trained generative model lands in the support of the distribution of the dataset, and recall is the probability that a sample from the dataset is within the support of the distribution of the trained generative model. Therefore, a generative model with high precision is able to generate a sample with high realism as the real data, and a high recall denotes the distribution learned by the generative model covers most part of the real distribution, resulting in high diversity generated results. Note that we adopt the evaluation code[22] of guided-diffusion (Dhariwal and Nichol 2021) to compute the precision and recall for generative models.

- For the analysis of the multi-scale vector quantization process, we consider the classical Peak signal-to-noise ratio (PSNR) and structural index similarity (SSIM) (Wang et al. 2004) as the reconstruction quality assessment, which are common metrics for evaluating

---

[20]torch-fidelity: https://github.com/toshas/torch-fidelity

[21]clipscore: https://github.com/jmhessel/clipscore

[22]guided-diffusion: https://github.com/openai/guided-diffusion

Hyper-parameter	CelebA-HQ (Frido-f8f4)	Landscape (Frido-f8f4)	LSUN-bed (Frido-f8f4)
	General settings		
Base learning rate	1e-6	3e-7	3e-7
Scale lr	False	True	True
Batch size	8	6	6
Training epochs	350	300	50
MS-VQGAN	MS-VQGAN-f8f4	MS-VQGAN-f8f4	MS-VQGAN-f8f4
Diffusion steps	1000	1000	1000
Noise scheduler	linear	linear	linear
Number of feature scales	2	2	2
	PyU-Net settings		
Model channels	224	192	192
Number of res blocks	2	2	2
Attention resolutions	2, 4, 8	1, 2, 4	1, 2, 4
Channel multiplier	1, 2, 3, 4	1, 2, 4	1, 2, 4
Number of heads	7	1	1
Noise ratio	0.1	0.1	0.1

Table B: Hyper-parameter settings for all *Frido* of all unconditional tasks, including unconditional image generation on CelebA-HQ, Landscape, and LSUN-bed. If model converges earlier, we used the checkpoint with best total ema loss.

Hyper-parameter	Model ablation (Fig.6)	Noise analysis (Fig.B)	Multi-scale analysis (Frido-f16f8, Table 6)	Multi-scale analysis (Frido-f8f4, Table 6)	Multi-scale analysis (Frido-f32f16f8, Table 6)	Multi-scale analysis (Frido-f16f8f4, Table 6)
	General settings					
Base learning rate	2e-7	4e-6	2e-7	2e-7	2e-7	2e-7
Scale lr	True	False	True	True	True	True
Batch size	32	32	32	6	12	2
Training epochs	120	120 (COCO/VG)	120	120	120	120
MS-VQGAN	MS-VQGAN f16f8	MS-VQGAN f16f8	MS-VQGAN f16f8	MS-VQGAN f8f4	MS-VQGAN f32f16f8	MS-VQGAN f16f8f4
Diffusion steps	1000	1000	1000	1000	1000	1000
Noise Schedule	linear	linear	linear	linear	linear	linear
Number of feature scales	2	2	2	2	3	3
	PyU-Net settings					
Model channels	192	192	192	192	192	192
Number of res blocks	2	2	2	2	2	2
Attention resolutions	2, 4, 8	2, 4, 8	2, 4, 8	2, 4, 8	2, 4, 8	2, 4, 8
Channel multiplier	1, 2, 3, 5	1, 2, 3, 5	1, 2, 3, 5	1, 2, 3, 5	1, 2, 3, 5	1, 2, 3, 5
Transformer depth	1	1	1	1	1	1
Number of heads	6	6	6	6	6	6
Context dim	640	640	640	640	640	640
Noise ratio	0.1	0.1	0.1	0.1	0.1	0.1
	Multi-modal Condition Encoding settings					
Encoding module	BERTEmbedder	BERTEmbedder	BERTEmbedder	BERTEmbedder	BERTEmbedder	BERTEmbedder
Number of layer	32	32	32	32	32	32
Attention embedding dim	640	640	640	640	640	640
Vocab size	30522	30522	30522	30522	30522	30522
Max sequence length	77	77	77	77	77	77

Table C: Hyper-parameter settings for *Frido* of all model analysis tasks. If model converges earlier, we used the checkpoint with best total ema loss.

the similarity between images. Also, we use *pytorch-gan-metrics*[23] to compute these metrics.

C.2 Datasets and Evaluation Setting

In this section, for reproducibility, we detail the evaluation setting for each task on each dataset.

- Text-to-image generation (T2I): We perform experiments of T2I on standard COCO setting (Zhou et al. 2022). In the standard T2I setting, models are trained on COCO 2014 captioning dataset only and evaluated on COCO 2014 validation set. In COCO 2014, the numbers of training and validation data are 83K and 41k, respectively. We note that, in the evaluation phase, models are evaluated on the full COCO 2014 validation set.

- Scene-graph-to-image generation (SG2I): We conduct experiments of SG2I on COCO and Visual Genome

datasets. For the COCO track, following the setting of sg2im (Johnson, Gupta, and Li 2018) and Canonicalsg2im (Herzig et al. 2020), we train our model on COCO 2017 Stuff Segmentation Challenge split, containing 25K/2K training/testing images. Also, we adopt the same pre-processing in sg2im to obtain the scene graph for each training image. In the Visual Genome dataset, the scene-graph-image pairs are given. In this paper, we use the same subset in sg2im, which ignores tiny objects and only uses images with 3 30 objects and 1+ relationships. This results in 62K/5K training/testing data. For the quantitative comparison, we also follow the evaluation protocol of previous works (Herzig et al. 2020; Jahn, Rombach, and Ommer 2021).

- Label-to-image generation: We evaluate the label-to-image models on COCO datasets. Following the evaluation protocol of (Jyothi et al. 2019; Yang et al. 2021), we use the 2017 Panoptic version of COCO, containing

---
[23]gan-metrics: https://pypi.org/project/pytorch-gan-metrics/

Figure B: More qualitative comparison on T2I on COCO. Note that the first row denotes the text conditions.

118K/5K training/validation images with bounding box annotations for each image (we only use image-level labels for training). For a better understanding of the performance on the scene image generation of different difficulties, we consider two settings on the validation sets. The first one is images with only 3-8 objects (total of 3,276 images), and the second one is validation images with 2-30 objects (total of 4,722).

- Layout-to-image generation: Similar to scene-graph-to-image generation, we perform the model training on COCO 2017 Stuff Segmentation Challenge split for a fair comparison with previous works. In the testing phase, we follow the common practice (Rombach et al. 2022; Sylvain et al. 2021; Jahn, Rombach, and Ommer 2021) and report the FID and IS on the testing set with 2,048 images. As for the OpenImage dataset, we follow the setting of VQGAN+T (Jahn, Rombach, and Ommer 2021) and sample 2,048 images in the validation set for evaluation.

- Unconditional image generation: We conduct unconditional image generation on LSUN-bed, CelebA-HQ, and Landscape datasets. For all datasets, we train our model with all the training sets without any filtering. In the evaluation phase, we follow common practice (Rombach et al. 2022; Anokhin et al. 2021; Casanova et al. 2021) to evaluate the performance on LSUN-bedand, CelebA-HQ, Landscape, where metrics are calculated between the 50k random generated images and the entire training set. Also, we use *torch-fidelity* to compute the FID score and utilize the script provided by ADM (Dhariwal and Nichol 2021) to obtain precision/recall scores.
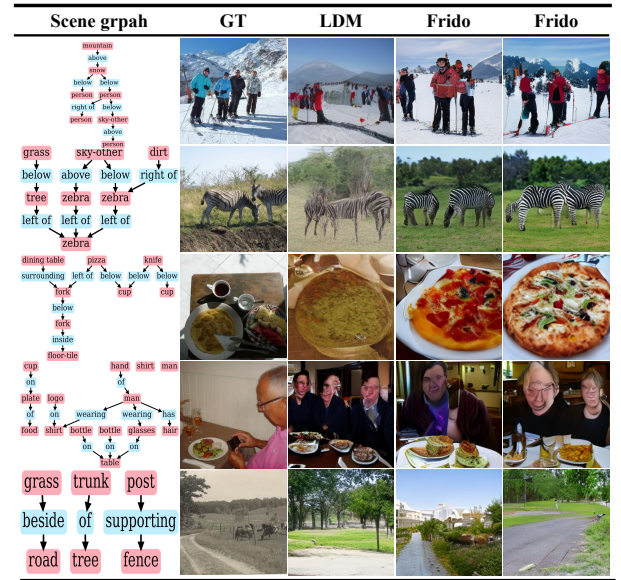

Figure C: More qualitative comparison on scene-graph-to-image generation.

Name	FID	Precision	Recall
DC-VAE	15.8	-	-
VQGAN+T. (k=400)	10.2	-	-
PGGAN	8.0	-	-
LSGM	7.22	-	-
UDM	7.16	-	-
LDM-4	**5.11**	**0.72**	0.49
Ours-f8f4	6.38	0.71	**0.50**

Table D: Unconditional image generation on CelebA-HQ.

D Additional Experiment Results

D.1 Conditional Image Generation

In this section, we provide more qualitative comparison results on various conditional image generation tasks, including text-to-image (Figure B), scene-graph-to-image (Figure C), label-to-image (Figure D), and layout-to-image (Figure E). Note that the settings of these qualitative experiments are the same as described in Section 4.2.

D.2 Unconditional Image Generation

To verify the generalizability of *Frido*, We also analyze the performance of our method on the unconditional image generation task, and compare *Frido* with previous works, including DC-VAE (Parmar et al. 2021), VQGAN (Esser, Rombach, and Ommer 2021), PGGAN (Karras et al. 2017), LSGM (Vahdat, Kreis, and Kautz 2021), UDM (Kim et al. 2022), CIPS (Anokhin et al. 2021), StyleGAN-v2 (Karras et al. 2020), ImageBART (Esser et al. 2021), DDPM (Ho, Jain, and Abbeel 2020), StyleGAN (Karras, Laine, and Aila 2019), ADM (Dhariwal and Nichol 2021), ProjectedGAN (Sauer et al. 2021), and LDM (Rombach et al. 2022). To this end, we train our model on CelebA-HQ,
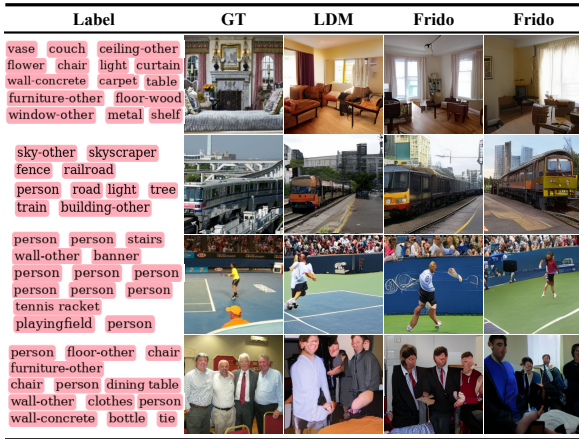
Figure D: More qualitative comparison on the label-to-image generation.

Name	FID	Precision	Recall
CIPS	3.61	-	-
StyleGAN-v2	**2.36**	-	-
LDM-4[†]	7.69	**0.69**	0.49
PyDM-f8f4	5.29	0.67	**0.51**

Table E: Unconditional image generation on Landscape 256.
[†] denotes models are trained by official code and configs.

LSUN-bed, and Landscape datasets, and evaluate these models with FID, Precision and Recall metrics to measure both the generated image quality and the coverage of the modeling data manifold. Table D, F, and E summary the results on CelebA-HQ, LSUN-beds, and Landscape, respectively. As can be seen in this table, we achieve comparable results in terms of image quality metrics (FID and precision). As for the coverage of the data manifold, we find that our model equips the diffusion model to learn the data manifold with high coverage, resulting in a high Recall rate. We contribute this to the feature pyramid design in the diffusion model, which leverages a coarse-to-fine learning strategy and allows DM to learn the dataset distribution easier. Moreover, we provide examples generated by *Frido* on these datasets, and the results on CelebA, Landscape, and LSUN-bed are shown in Figure F, G, and H, respectively.

D.3 Model Analysis

Computation Cost Continued from Section 4.3, we report the computation cost for each ablated version of *Frido* and compare it with the previous latent diffusion model, LDM (Rombach et al. 2022), in terms of FLOPs, parameter counts, and inference time. As shown in Table G and Figure 6 in the main paper, we demonstrate that *Frido* is able to boost the performance for all metrics with only a minor increase in parameter count (total of 697M). As for the inference time, we set the total timesteps to 200s for both LDM and *Frido* and report the inference time (sec) per image. In this table, we can find that under the same infer-
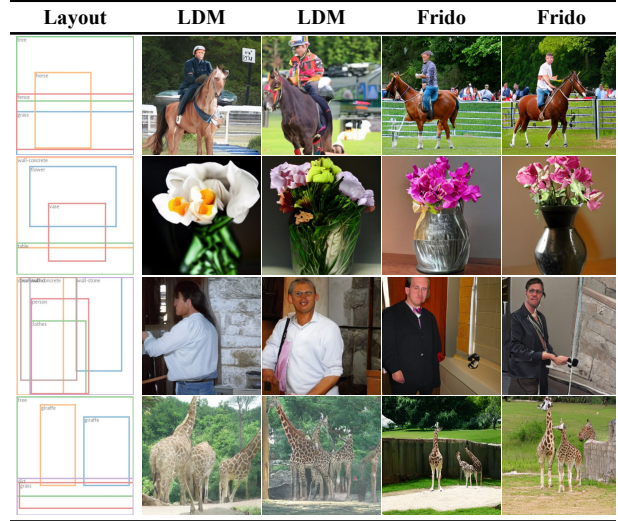

Figure E: More qualitative comparison on the layout-to-image generation. Note that the layouts are from the paper of LDM (Rombach et al. 2022).

Name	FID	Precision	Recall
ImageBART	5.51	-	-
DDPM	4.9	-	-
UDM	4.57	-	-
StyleGAN	2.35	0.59	0.48
ADM	1.90	**0.66**	**0.51**
ProjectedGAN	**1.52**	0.61	0.34
LDM-4	2.95	**0.66**	0.48
PyDM-f8f4	3.87	0.64	**0.51**

Table F: Unconditional image generation on LSUN-Beds.

ence timestep setting, *Frido* achieve comparable inference cost per image compared with LDM, while as shown in Figure 7, *Frido* achieves decent performance improvement on both tasks. This again verifies the efficiency of *Frido* in high-quality conditional image generation.

E Additional Discussion

E.1 Limitations and Future Directions

We observed that the distribution of the encoded features (by MS-VQGAN) at each scale is not regularized, resulting in large variations in the mean and standard deviation of features at different scales. This could further bring negative effects on the learning of the diffusion model. Specifically, in the diffusion process, the noisy data are created by interpolating input features with standard normal variations, requiring the distribution of input features to better be with mean$\approx$0 and std$\approx$1. Therefore, the non-regularized input features may not be corrupted into noise in the diffusion process as expected, damaging the learning of the denoising process. In this paper, we mitigate this problem by scaling each scale of feature independently with the reciprocal of the standard deviation of the corresponding feature. How-

Method	FLOPs	Params	Inference time (sec/img)
LDM-8	37.1 G	589.8 M	0.82547
Baseline	37.3 G	1.179 B	1.02865
+ PyU-Net	31.7 G	589.8 M	0.75052
+ Coarse-to-fine gating	39.7 G	697.8 M	0.91782

Table G: Model ablation of T2I on COCO. The inference time is estimated on single V100 with 32 batch-size. Also, the total inference timesteps are 200s for both LDM and *Frido*.

ever, we believe that a regularization objective is needed to constrain the distribution of the encoded latent in such a quantization process for the diffusion model.

Another potential future direction is to explore the question of "what kind of high or low knowledge encoded in the features would benefit the coarse-to-fine learning of the diffusion model?". In *Frido*, we design multi-scale VQGAN with a feature pyramid fusion module, enabling us to encode an input image into features with multiple scales and extract high and low-level information implicitly. To explore the aforementioned question, we may enhance MS-VQGAN by adding an objective function to guide the information extracted on high or low-level features. Specifically, a reconstruction loss between the low resolution of the input image and the reconstructed image decoded by only high-level features may be imposed to MS-VQGAN to guide the multi-scale quantization explicitly. We will leave these directions for future research.

E.2 Ethics Concerns

Similar to other generative works, *Frido* would be also vulnerable to *malicious* use because of its powerful ability to generate real-world images based on complex cross-modal conditions, ranging from the label, natural language, bounding box layout, and scene graph. Moreover, the *fairness* for generating particular categories of objects (e.g., human) would be a potential problem for generative models used in a real-world scenario. We contribute such social bias to the potential data collecting bias in the training datasets. Such potentially social issues had been identified and discussed in the recent works (Tan, Shen, and Zhou 2020), and some possible solutions to mitigate these problems are considered in a survey (Brundage et al. 2018).

Unconditional image generation on CelebA 256x256

Figure F: Generated examples of unconditional image generation on CelebA 256x256.

Unconditional image generation on Landscape 256x256
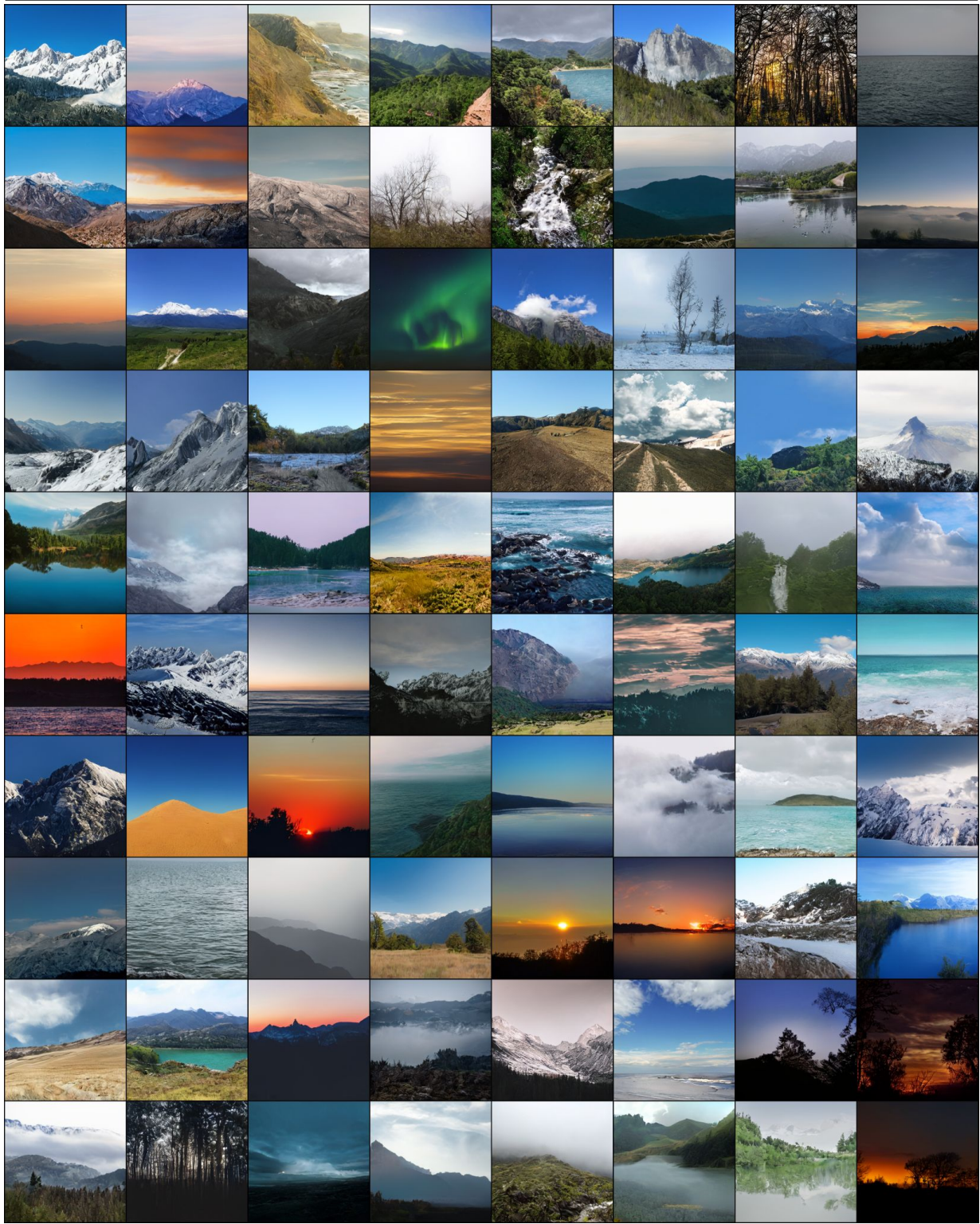

Figure G: Generated examples of unconditional image generation on Landscape 256x256.

Unconditional image generation on LSUN-bed 256x256

Figure H: Generated examples of unconditional image generation on LSUN-bed 256x256.